sustainability

MDPI

Article

Numerical Simulation and Design of Multi-Tower Concentrated Solar Power Fields

Zaharaddeen Ali Hussaini [1,2,*], Peter King [1] and Chris Sansom [1]

[1] School of Water Energy and Environment, Cranfield University, Cranfield MK43 0AL, UK; peter.king@cranfield.ac.uk (P.K.); c.l.sansom@cranfield.ac.uk (C.S.)
[2] Centre for Renewable Energy Research, Bayero University, Kano 700241, Nigeria
* Correspondence: zaharaddeen-ali.hussaini@cranfield.ac.uk or zee.18us@live.com

Received: 7 February 2020; Accepted: 10 March 2020; Published: 19 March 2020

Abstract: In power tower systems, the heliostat field is one of the essential subsystems in the plant due to its significant contribution to the plant's overall power losses and total plant investment cost. The design and optimization of the heliostat field is hence an active area of research, with new field improvement processes and configurations being actively investigated. In this paper, a different configuration of a multi-tower field is explored. This involves adding an auxiliary tower to the field of a conventional power tower Concentrated Solar Power (CSP) system. The choice of the position of the auxiliary tower was based on the region in the field which has the least effective reflecting heliostats. The multi-tower configuration was initially applied to a 50 MWth conventional field in the case study region of Nigeria. The results from an optimized field show a marked increase in the annual thermal energy output and mean annual efficiency of the field. The biggest improvement in the optical efficiency loss factors be seen from the cosine, which records an improvement of 6.63%. Due to the size of the field, a minimal increment of 3020 MWht in the Levelized Cost of Heat (LCOH) was, however, recorded. In much larger fields, though, a higher number of weaker heliostats were witnessed in the field. The auxiliary tower in the field provides an alternate aim point for the weaker heliostat, thereby considerably cutting down on some optical losses, which in turn gives rise to higher energy output. At 400 MWth, the multi-tower field configuration provides a lower LCOH than the single conventional power tower field.

Keywords: concentrated solar power; field layout; heliostat field; multi-tower field

1. Introduction

Due to the declining patronage of nuclear energy and volatile petroleum and natural gas prices, coupled with the rising global temperature, predominately due to the atmospheric build-up of CO_2, nations at large are opting for and considering renewable energy technologies for their power generation. Solar energy, in particular, is seen as an extremely viable option, especially in areas with good solar insolation [1]. Solar thermal energy for electricity generation is typically referred to as Concentrated Solar Power (CSP) [2]. CSP can be a driving force in the cause of reducing CO_2 emission, thereby contributing to reducing and limiting the global temperature increase. Of the existing types of CSP, power tower systems are one of the most promising solar thermal technologies. This is mainly due to their ability to offer higher temperatures and, hence, higher efficiencies [2–7].

In power tower systems, the heliostat field is one of the essential subsystems. This is due to its significant contribution to the plant's total investment cost: about 40%–50% of the plant's cost is attributed to the heliostat field [8–12]. The field contributes equally to the plant's overall power losses of about 40% [8,13–16]. It has hence become essential to ensure that the field layout is optimal at collecting energy from the sun. The design and optimization of the heliostat field is hence an active area of research, with new field improvement processes being actively investigated. Several methods have been proposed in the literature to improve heliostat field efficiencies and reduce losses, either by improving through optimization or by suggesting new heliostat field layout patterns and configurations entirely.

Several literatures that focus on heliostat field layout patterns and configurations are available. In Noone et al.'s [8] work, for example, a spiral field pattern inspired by disc phyllotaxis is introduced, which is applied in heliostat field design and optimization. By redesigning the layout of the PS10 field using the algorithm, an improvement in the optical efficiency and a reduction in the land area utilized is witnessed. E. Carrizosa et al. [17] presented a pattern-free heliostat field layout distribution style, obtained by the simultaneous optimization of both the heliostat field (heliostat locations and number) and the tower (tower height and receiver size). Cadiz et al. [10] presented shadowing and blocking optimization procedures for a variable-geometry heliostat field. The variable-geometry concept explored by the author allows the possibility of minimizing the cosine losses by rotating the entire field. In a similar vein, Mohammed Aldulaimi and MS Soylemez [14] suggested a new heliostat field layout arrangement by identifying heliostats with low optical efficiency and increasing their heights in a bid to curb blocking losses and hence increase the total annual field efficiency. Emilo Carrizosa [18] also suggested some alterations in the field by considering a field with different heliostat sizes. Mani Yousefpour Lazardjan [19] presented a tool developed at Solar-Insitut Julich (SIJ) primarily for the optimization of a novel micro-heliostat concept. In a novel and unconventional heliostat field layout design, Danielli et al. [20] developed the concatenated micro-tower (CMT). In this configuration, dynamic receivers mounted on arrays of small towers enable heliostats in mini subfields to direct sunlight with minimal cosine losses, thus improving the field's overall optical efficiency. N. Cruz et al. [21] also developed an algorithm using a genetic algorithm that generates a continuous pattern-free field layout. The algorithm developed, using parallelization, provides a solution to the conceptual complexity and high computational cost associated with pattern-free heliostat field optimization. Arrif et al. [22] also developed an algorithm which is based on the bee colony optimization method to optimize the case study site of the PS10 CSP power plant in Spain. The proposed algorithm, the Artificial Bee Colony Algorithm (IABCA), finds the best position for each heliostat on the field in which the maximum efficiency for both the heliostat and field is reached within a limited area. L Deng et al. [23] proposed a new pattern for the heliostat field layout: a rose pattern based on the classic radial staggered configuration. The pattern divides the radial staggered configuration into six sectors, and some of those sectors are then optimized separately using advanced differential equation algorithm, thus increasing the optimization variables. In another unconventional heliostat field layout design, additional towers, each having its receiver mounted atop, are introduced in the field.

Although it is only recently that the multi-tower setup has attracted much interest in the research community, the configuration has been explored in the past. In 1999, Romero et al. [24] pointed out that centralized large solar power tower plants are at odds with the increasing shift towards a distributed-energy setup and could hence face future deployment difficulties. They proposed and analyzed how small tower fields could be integrated into a Modular Integrated Utility Systems (MIUS) approach, in order to fully exploit the advantages of a distributed-energy setup in a community. In 2002, Schramek and Mills [25] proposed a Multi-Tower Solar Array (MTSA) system, which consists of a collection of solar towers densely grouped together, thereby allowing for partial overlapping of the heliostats in the field, and hence allowing greater utilization of the solar radiation falling on the unused ground area in the field. In a more recent work, in 2012, Augsburger and Favrat [26] proposed a method in which each individual heliostat is instantaneously aimed at a receiver in a multi-tower setup, following an aim selection criterion. The thermo-economic performance of a three-tower heliostat field was then evaluated using a model. In another work, eSolar and Inc. (B&W PGG) [27] investigated the use of small heliostats with multiple receivers and towers [27]. They proposed a configuration with 14 molten salt power towers, for a 100 MWe (net) power block that is capable of delivering a

75% capacity factor. Tyner and Wasyluk [28] presented a follow-through on the conceptual design previously developed by eSolar and Inc., where several trade studies were carried out in order to arrive at the optimally cost-effective system configuration for the multi-tower setup. The concept proposed involves replicating the field, without scaling or redesign, in order to meet the capacity required. In another work by Pasha Piroozmand and Mehrdad [29], an iterative algorithm was developed in order to obtain the optimum instantaneous efficiency of the heliostat in the field when selecting the tower which radiation will be reflected onto in a two-tower field set up, so as to maximize the annual optical efficiency of the field. As a case study, the authors used Particle Swarm Optimization (PSO) to optimally design a two-tower spiral patterned field along the east-west line before redesigning the field using the iterative method. The authors here noted that issues such as field layouts and aiming strategies need to be further investigated in order to achieve a more optimized and comprehensive multi-tower system. In 2018, Vast Solar, an Australian company engaged in CSP research, developed and commissioned a 1.1MWe pilot plant utilizing a modular solar array field [30]. Each of the five modular arrays in the field has a dedicated tower in which the Heat Transfer Fluid (HTF) is heated at the receiver. The multiple towers are connected to a central thermal storage unit. The company is already planning to go further by developing a 30MW commercial demonstration project in Australia using the modular array field.

In all the multi-tower configurations reviewed, each tower has its own heliostat field, which replaces an entire field with surrounding heliostats in smaller units until the capacity required is met. In this paper, a different architecture of the multi-tower configuration is investigated. The configuration explored, which provides an alternate viewpoint to the usual mainstream multi-tower configuration, involves adding an auxiliary tower to an existing surrounding field. The paper initially begins by defining the models used for the development of a conventional heliostat field. After model validation, a 50 MWth solar field was simulated in Nigeria, with the objective function being the Levelized Cost of Heat (LCOH). An auxiliary tower was then added onto the existing field, and its effects investigated. The results from the optimized multi-tower configuration were then compared with conventional fields at different thermal field powers, in order to determine the optimum transition size from a single field to a multi-tower field.

2. Model Description

2.1. Solar Insolation, Time and Angles

Finding the position of the sun is one of the very first steps that needs to be taken. The position can be characterized by the altitude (α) and azimuth angle (γ_s). Figure 1 shows the angles defining the apparent position of the sun [12,31].

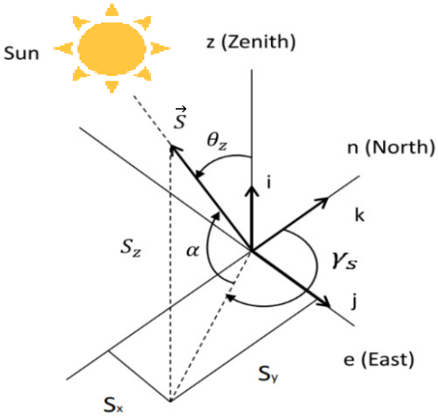

Figure 1. Position of the sun relative to the collector.

Where θ_z is the zenith angle and S_x, S_y, and S_z denote the vector components $\overrightarrow{S}$ of the sun's radiation. The solar altitude is given by Equation (1) [31]:

$$\mathrm{Sin}\alpha = \mathrm{Sin}\varphi\mathrm{Sin}\delta + \mathrm{Cos}\varphi\mathrm{Cos}\delta\mathrm{Cos}\omega \tag{1}$$

where latitude, φ, is angular location relative to the equator, and declination angle, δ, is the angular position of the sun at solar noon on the equatorial plane. The declination angle is given by Equation (2):

$$\delta = 23.45\mathrm{Sin}\left(360 \times \frac{284 + n}{365}\right) \tag{2}$$

where n represents the day number of the year [31], and ω is the Hour angle (east or west angular displacement of the sun about the local meridian due to earth's rotation about its polar axis). It is represented in Equation (3), with t being the solar time [31].

$$\omega = 15 \times (t - 12) \tag{3}$$

The azimuth angle, on the other hand, is given by Equation (4) [31]

$$\mathrm{Sin}\gamma_s = \frac{\mathrm{Cos}\delta\mathrm{Sin}\omega}{\mathrm{Cos}\alpha} \tag{4}$$

Specific geographical locations in Nigeria are highly suitable for the deployment of solar energy technologies, especially in the northern parts of the country. For regions in the northern parts of Nigeria, a Direct Normal Irradiance (DNI) average value of around 5.5 $kWh/m^2/day$ is obtainable [32–34], making the area suitable for CSP deployment. The solar insolation at the selected site, Katsina, Nigeria (Latitude: 12.39° N Longitude: 7.60° E), was obtained from the metrological agency in Nigeria, NiMet (Nigerian Metrological Agency). The DNI at the identified site averages out to 5.53 kWh/m^2/day.

2.2. Optical Efficiency

The optical efficiency of the field measures the capability of each heliostat to concentrate and reflect radiation to the receiver. Every heliostat has a particular optical efficiency value due to its position in the field and its interaction with the other elements in the field. The overall value for the field is then calculated by averaging each particular result. The optical field efficiency is expressed by Equation (5) [8,12,35];

$$\eta_{field} = \eta_{cos} \times \eta_{sb} \times \eta_{att} \times \eta_{int} \times \eta_{ref} \tag{5}$$

where η_{cos}, η_{sb}, η_{att}, η_{int}, and η_{ref} represent losses due to cosine, shadowing and blocking, atmospheric attenuation, interception and mirror reflectivity factors, respectively. Maximizing field efficiency is an important task that ensures the optical losses are reduced as much as possible.

2.2.1. Cosine Efficiency Loss

The cosine efficiency loss is one of the most critical energy loss sources in heliostat fields and often represents the most significant loss term [36]. It is defined as the cosine of the angle formed by the incident solar beam radiation and the vector normal to the reflective heliostat surface [37]. The efficiency factor depends on both the position of the sun and of the heliostat [12]. Figure 2 shows the effect of cosine on reflected rays from the heliostat.

To evaluate the normal vector of the heliostat surface, two other vectors need to be defined, i.e., the vectors from the center of the heliostat to the sun, $\overrightarrow{S}$, and those to the desired image location on the receiver surface, $\vec{r}$. Assuming x, y, and z are the coordinates of the heliostat center, and TH is the tower height, the components of the unit vector of the reflected ray, $\vec{r}$ is given by Equation (6) [38,39]:

$$\vec{r} = \left[\frac{-x}{\sqrt{x^2 + y^2 + (TH - z)^2}}, \frac{-y}{\sqrt{x^2 + y^2 + (TH - z)^2}}, \frac{(TH - z)}{\sqrt{x^2 + y^2 + (TH - z)^2}} \right] \tag{6}$$

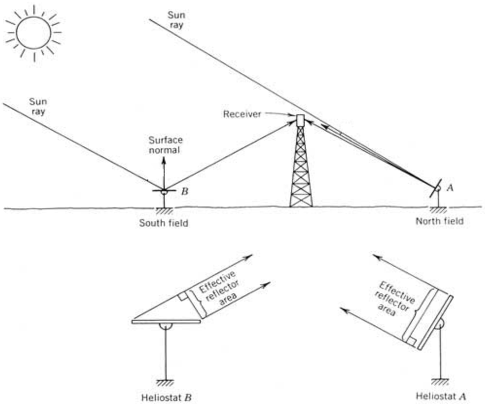

Figure 2. Figure showing the effect of cosine on reflected rays in Heliostat A and B.

Vector $\vec{S}$ components are formed from Figure 1. With $\vec{S}$ and $\vec{r}$ defined, the components of the unit vector normal of the heliostat surface can then be evaluated (Equation (7)):

$$\vec{m} = \frac{\vec{S} + \vec{r}}{\left|\vec{S} + \vec{r}\right|} \tag{7}$$

The cosine efficiency can now be calculated as the dot product of the unitary vectors $\vec{m}$ and $\vec{S}$, as shown in Equation (8):

$$\eta_{cos} = \vec{m} \cdot \vec{S} \tag{8}$$

2.2.2. Shadowing and Blocking Efficiency Loss

Shadowing and blocking losses are a result of the reduction of the heliostat's useful area due to the presence of a heliostat in the path of the incident radiation or to reflected radiation, respectively. In Figure 3, the contour of the representative heliostat and the projected contour of the two adjacent heliostats in a radial staggered configuration is shown.

Here, bh and bw are the blocking and shadowing portions of the representative heliostat. LH and LW are the heliostat's length and width, respectively. DM is the diameter of the heliostat, inclusive of dsep (the extra security distance between adjacent heliostats).

The blocking and shadowing model adopted the simplified calculation method developed by Sassi [40], using the outline projections of the neighboring heliostats. This method divides the surfaces of each heliostat into strips, and those strips identified to have potential for shadowing and blocking are projected onto the surface of the problem heliostat. Among all the shading and blocking projections, the maximum height is selected for each strip. The fraction of the area free from shading and blocking gives the shading and blocking efficiency value.

As to the identification and selection of the shadowing and blocking heliostats, the method outlined in [37] by Besarati and Goswami is adopted. This methodology considers only a subset of the heliostats that have a high potential for shadowing and blocking. For shading, a circle of radius

$R_{sb} = 2.5DM$ is initially drawn around the centre of the analyzed heliostat. The vector connecting the centre of the analyzed heliostat is then projected to the sun on the horizontal plane. The heliostats near the projection are identified to have the highest potential to shade and thus selected for the analysis.

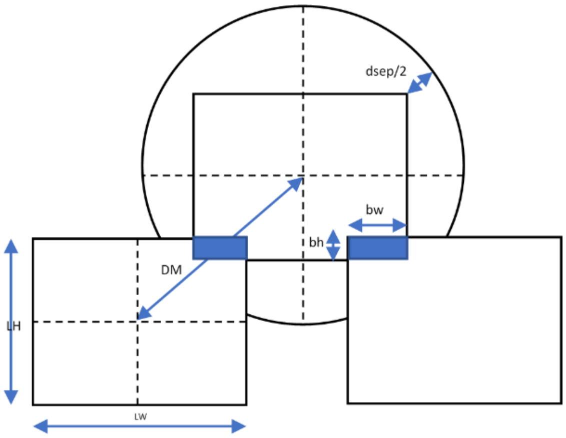

Figure 3. Blocking showing the contour of the representative heliostat and the projected contour of two adjacent heliostats in the first-row.

With the radial staggered configuration (the adopted field layout generation methodology), the method from Besarati and Goswami is not required for the identification of the blocking heliostats, as this can quickly be done by considering the 'shoulder' heliostats at the next row (Figure 3) of the analyzed heliostat and the one that is two rows over and directly in front of it [41].

2.2.3. Attenuation Efficiency Loss

The radiation reflected from the heliostat does not wholly reach the receiver. This is because some energy is scattered and/or absorbed by the atmosphere. Atmospheric attenuation consists of energy losses in the reflected radiation during passage through the atmosphere from each heliostat to the receiver. This is an efficiency factor that is typically dependent on the distance of the heliostat relative to the tower, the aerosol distribution at the ground level, and site altitude [42]. On a day when visibility is good, the energy loss will be a small percentage of the energy loss per kilometer. This atmospheric attenuation efficiency can be calculated using Equation (9), as provided in [43], for fields with a distance between heliostat and receiver aim point below 1000 m:

$$\eta_{att} = 0.99321 - 0.0001176D + 1.97 \times 10^{-8} \times D^2 \; D \leq 1000m \tag{9}$$

The formula in Equation (9) was extended by M.Schmitz et al. [44] For larger fields, see Equation (10):

$$\eta_{att} = exp(-0.0001106D) \; D > 1000m \tag{10}$$

where D is the distance between the heliostat and the aim point of the receiver.

2.2.4. Interception Efficiency Loss

The interception efficiency loss, otherwise known as spillage, refers to reflected energy directed towards the receiver that does not fall on the absorbing area. The factor is dependent on both the heliostats in the field and the receiver design and properties [12]. While the 'spill' of the reflected radiation can be reduced by increasing the receiver size, consideration of other receiver energy losses and receiver costs must be made. A description of the spilled radiation is shown in Figure 4. The spillage can be calculated by integrating the image shape produced by the mirror over the receiver domain [44–48].

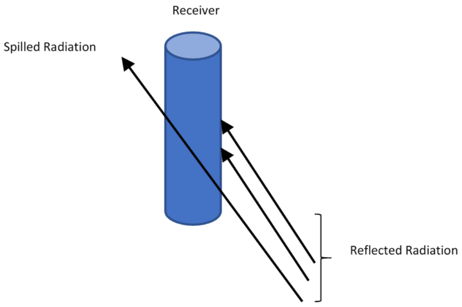

Figure 4. A demonstration of spillage on the receiver.

The University of Zaragoza (UNIZAR) [46] and HFLCAL [48] methods are widely used for the analytical expressions of interception efficiency and appropriate tools for design and optimization. The HFLCAL model, from the German Aerospace Centre (DLR), is applied in this paper. The model is adjudged to be both simpler and slightly more accurate that the UNIZAR method [47]. The HFLCAL model's flux density expression is a circular normal distribution. The efficiency loss is expressed by Equation (11) [44,48];

$$\eta_{int} = \frac{1}{2\pi\sigma^2{}_{tot}} \int_{x'}\int_{y'} exp\left(\frac{-x^2+y^2}{2\sigma^2{}_{tot}}\right)dydx \tag{11}$$

where x' and y' are coordinates of the plane normal to the receiver surface and σ_{tot} is the standard deviation of the flux distribution on the receiver plane given by Equation (12) [44];

$$\sigma_{tot} = \sqrt{D^2(\sigma^2{}_{tot} + \sigma^2{}_{bq} + \sigma^2{}_{ast} + \sigma^2{}_{tr})} \tag{12}$$

where σ_{sun}, σ_{bq}, σ_{ast}, σ_{tr} are the standard deviations due to sun shape error, mirror slope error, astigmatic error, and tracking error, respectively. A sun shape error value of 2.51 mrad, as measured in Planta Solar Almeria (PSA) [41], is applied here. The beam quality value is assumed to be 1.88 mrad, as reported in [49]. Also, as in [49], the σ_{tr} is assumed at 0.63, a value obtained from tests on the SENER heliostat under low wind conditions. The astigmatism effect σ_{ast}, can be calculated by Equation (13) [44];

$$\sigma_{ast} = \frac{\sqrt{0.5(H_t^2 + W_s^2)}}{4D} \tag{13}$$

where H_t and W_s are the image dimensions in the tangential and sagittal planes at the receiver position. The values are given by Equation (14) [44];

$$H_t = \sqrt{LW + LH}\left|\frac{D}{f} - \text{Cos}\varepsilon\right|, W_s = \sqrt{LW + LH}\left|\frac{D}{f}\text{Cos}\varepsilon - 1\right| \tag{14}$$

where f is the focal distance of the heliostat surface and $Cos\varepsilon$ is the incidence cosine between the sunrays and the heliostat normal.

2.2.5. Mirror Reflectivity Loss

Mirror reflectivity affects the amount of radiation that can be redirected by the heliostat. This is primarily due to the design specifications and condition of the heliostat. A uniform reflectivity value of 0.88 is adopted here, as in [8,49]. The reflectivity efficiency can hence be fully expressed as:

$$\eta_{ref} = 0.88 \times (0.95) \tag{15}$$

where the 0.95 factor is the nominal value adopted for cleanliness. In this work, the η_{ref} is assumed constant for all heliostats in the field.

2.3. Field Layout Model

In this paper, the proposed method for the field layout and generation is the radial staggered distribution. The configuration provides a well-established and tested methodology for the generation of a heliostat field. The radial staggered arrangement ensures that no heliostat is placed directly in front of another heliostat in adjacent rings. In this way, a reflected beam from any heliostat passes between its adjacent neighbors on the way to the receiver [50]. Figure 5 shows a typical representation of the radial staggered configuration [38].

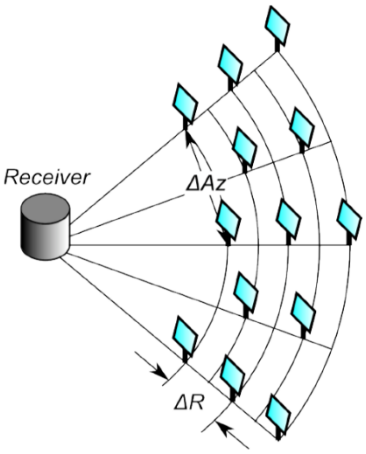

Figure 5. Radial staggered configuration.

The method for the generation of the radial staggered layout presented in [13] (campo) is applied here. One of the purposes of this code, developed by FJ Collado, is to improve the accuracy and speed with which the heliostat field is optimized and designed. This makes it convenient for the intended application here. Details of the campo steps are outlined in [13,51].

The field is initially laid out by developing the densest field made up of concentric rows of heliostats. The field is gradually expanded by altering the radial separation distances, ΔR, during the optimization process. The parameters in the layout of the field are shown in Figure 6.

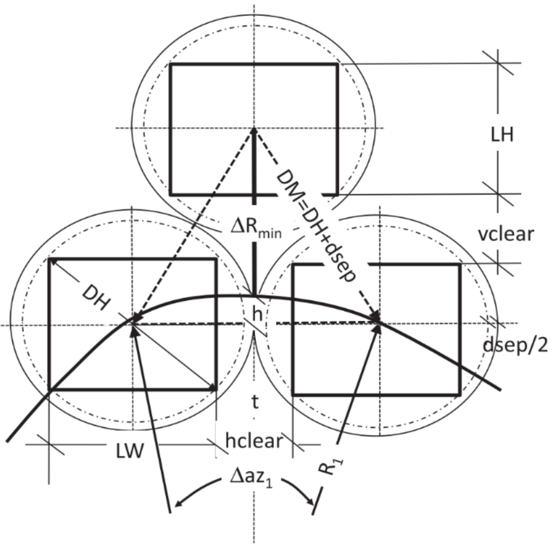

Figure 6. Parameters defining the layout of the field.

The densest field has ΔR_{min}, with the minimum radial increase at:

$$\Delta R_{min} = DM\ Cos30\ ^{\circ} \tag{16}$$

where DM is the horizontal clearance, *dsep*, added to the heliostat diagonal length (DH).

$$DM = DH + dsep \tag{17}$$

The heliostat field layout procedure for generating the heliostat configuration begins by placing the first heliostat tangential to the Y-axis (North) at radius distance R1 from the center, where the tower is situated. The second heliostat is placed at the same radius distance, at an azimuth angle distance, Δaz_1, from the initially placed heliostat. This placement continues through the entire row. This process is continued on subsequent rows of the field, with the first row being odd and the second row even (starting point here is at the Y-axis), in order to provide the needed staggered configuration. The azimuthal distance Δaz_1, can be expressed by Equation (18):

$$\Delta az_1 = 2\mathrm{Sin}^{-1}\left(\frac{DM}{2R1}\right) \tag{18}$$

R1 can be determined by the following:

$$R1 = Nhel_1\left(\frac{DM}{2\pi}\right) \tag{19}$$

where $Nhel_1$ is the number of heliostats in the first row.

As the consecutive rows are increased, the distance between the heliostats widens until it eventually becomes higher than DM. At his point, a new zone is created in which layout generation is started afresh. The number of zones in this developed model is limited to three.

In the new zone, the radius from the tower can be calculated by;

$$R_i = 2^{i-1}\left(\frac{DM}{\Delta az_1}\right) \tag{20}$$

where i signifies the subsequent zones in the field. The angular spacing in the *i*th zone in the field can also be determined by:

$$\Delta az_i = \left(\frac{\Delta az_1}{2^{i-1}}\right) \tag{21}$$

With the field layout generated, expansion and optimization of the field can then be initiated. In this particular model, the optimization is not only limited to improving the optical efficiency but also obtaining the parameters of the field. The parameters of the field constitute the design variables (namely, the number of heliostats in the first row, heliostat area, tower height, and consecutive row separation distance in the first, second, and third zones). The design variables are optimized using a Genetic Algorithm (GA) within the context of the chosen objective function to arrive at the required field thermal power. The model is developed using the computer programming language MATLAB developed by MathWorks.

Model Validation

Table 1 compares the results presented in the reference model, campo, by F.J Collado [49] to those of the one developed here. The campo model uses data and references from the Gemasolar plant in Sevilla, the first commercial plant with molten salt storage. The field data and specifications used for model validation in the Gemasolar plant are outlined in [49].

Table 1. Model results in comparison to campo method.

Zones	**Zone 1**			**Zone 2**			**Zone 3**		
	Field Efficiency								
Row Spacing (m)	**Ref Model (%)**	**Model (%)**	**Diff (%)**	**Ref Model (%)**	**Model (%)**	**Diff (%)**	**Ref Model (%)**	**Model (%)**	**Diff (%)**
ΔR1 = 0.866DM	65.34	65.21	0.20	55.42	55.12	0.54	37.54	37.34	0.53
ΔR2 = 0.866DM									
ΔR3 = 0.866DM									
ΔR1 = 0.866DM	65.36	65.21	0.23	58.45	58.59	−0.24	48.05	47.79	0.54
ΔR2 = 1.4DM									
ΔR3 = 1.4DM									
ΔR1 = 0.866DM	65.36	65.21	0.23	57.85	57.86	−0.02	48.35	48.27	0.17
ΔR2 = 1.6DM									
ΔR3 = 1.6DM									
ΔR1 = 0.866DM ΔR2 = 1.4DM	65.36	65.21	0.23	58.66	58.79	−0.22	50.26	49.98	0.56
ΔR3 = 1.6DM									
ΔR1 = 0.866DM	65.36	65.21	0.23	58.77	58.89	−0.20	51	50.78	0.43
ΔR2 = 1.4DM									
ΔR3 = 1.8DM									
ΔR1 = 0.866DM	65.36	65.21	0.23	58.75	58.89	−0.24	51.07	50.69	0.74
ΔR2 = 1.4DM									
ΔR3 = 2.0DM									
ΔR1 = 0.866DM	65.36	65.21	0.23	58.68	58.89	−0.36	50.9	50.58	0.63
ΔR2 = 1.4DM									
ΔR3 = 2.2DM									

The results in Table 1 show that all the field efficiency values are within a 1% margin difference. The differences can be attributed to the solar radiation data used. Although the data is from the same location in Seville, Spain, the reference model uses Typical Meteorological Year (TMY) data. The model developed, due to unavailability of data, utilizes measured data for a limited period (the years 2013–2014). The difference may also be a result of the optical loss model for shadowing and blocking utilized, which differs from the one used in the reference model.

3. Design and Optimization

3.1. Conventional Field

The validated model was then applied to the selected site in order to design and optimize, initially for the conventional field, a 50 MWth field. As earlier stated, the field in power tower systems has a significant weighting effect on the overall plant efficiency. This, in addition to being the most expensive part of the plant, further necessitates the importance of optimization in designing the heliostat field layout.

In this work, the primary objective function considered in optimization was in the form of minimizing a simplified Levelized Cost of Heat given by Equation (22) [52–54]. In calculating LCOH, only an independent generating system was assumed:

$$\frac{Total\ Heliostat\ Field\ Life\ Time\ Cost}{Total\ Life\ Time\ Output\ of\ Annual\ Thermal\ Energy\ Generated\ at\ Receiver\ Surface} = \frac{Field\ Installed\ Cost{*}CRF}{E_{th}} + O\&M \tag{22}$$

where O&M signifies the operating and maintenance cost, and CRF is the uniform series capital recovery factor. The CRF is given by

$$CRF = \frac{ir(1+i)^N}{(1+ir)^N - 1} \tag{23}$$

where N is the lifespan of the project, and ir is the interest rate. The lifespan of the project was assumed to be 25 years with a lending rate of 9%, values similar to those adopted in [55]. This equates the CRF to 0.1018.

A report by the International Renewable Energy Agency (IRENA) in 2014 [56] puts the total O&M of an entire CSP plant between 0.02 and 0.04 $/kWh. For the purpose of this paper, because the work was limited only to the heliostat field and thermal power, the lower end of the spectrum (0.02 $/kWht), was taken as the O&M cost.

The annual thermal energy at the receiver's aperture, E_{th} is given by the summation of the product of the instantaneous optical efficiency value for each heliostat, heliostat area, and the instantaneous beam radiation befalling an individual heliostat for all heliostats in the field (this also represents the power sent out from each individual heliostat). The power from each heliostat is then summed over the beam radiation at all sunshine hours on a representative day of the month [31], I_day. This is done for all months in the calendar year. Equation (24) describes the annual thermal energy at the receiver surface:

$$E_{th} = \sum_{1}^{Hel}\left[\sum_{I\_day}^{Year} \eta_{hel} \times I \times A_h\right] \tag{24}$$

where A_h is the heliostat area, η_{hel} is the instantaneous heliostat optical efficiency, I is the instantaneous beam radiation during sunshine hours, and Hel is the number of heliostats in the field. Only some days in the year are recommended to be used as average days for the month, and those were used in this work. The total heliostat field cost is a function of the tower cost, receiver cost, and heliostat cost. The cost model utilized in the National Renewable Energy Laboratory's (NREL) System Advisor Model (SAM) is applied here [57–59]. The system cost in SAM is limited only to direct capital costs.

As an example, the computed value for the LCOH in the Gemasolar plant (using Equation (22) with heliostat field cost at $114,260,000 and E_{th} at 408.330 GWht, as depicted in [55]) is 0.0485 $/kWht. This result assumes a CRF value of 0.1018 and O&M at 0.02 $/KWht.

The optimization code was developed using GA [37,60,61]. This algorithm uses the design variables (Table 2) to calculate the objective function. The algorithm picks the design variables randomly and uses them as parents to produce the children for the next generation in achieving the optimal solution. In order to reduce computational expense, lower and upper bounds for the design variables are set during optimization. The variables are initially made to assume the values of the Gemasolar plant.

Table 2. Conventional Field Model design variables with lower and upper bounds.

Design Variables	Variables Range
Number of Heliostats in 1st row (Zone 1)	10–46
Heliostat Area (m^2)	25–120
Receiver Dimensions (m^2)	25–226
Tower Height (m)	25–140
Heliostat Row Separation Distance Zone 1 (m)	(0.866 − 1.666) × DM
Heliostat Separation Distance Zone 2 (m)	(0.866 − 2.666) × DM
Heliostat Separation Distance Zone 3 (m)	(0.866 − 3.666) × DM

One of the defining constraints in the optimizer is the thermal power of the field. With a random selection of design variables, it is possible to reach a value that is below or above the set goal of 50

MWth. The optimizer is then made to disregard such results from the population. The results of the conventional field from the optimization in the model developed are summarized in Table 3.

Table 3. Summary of key results from the 50 MWth Conventional Power Tower field from the model developed and System Advisor Model (SAM).

Parameter	Model	System Advisor Model (SAM)
Heliostat Area (m^2)	95.17	95.17
Central Tower Height (m)	91.48	83.98
Central Receiver Area (m^2)	55.84	91.43
Levelized Cost of Heat, LCOH ($/kWht)	0.0474	0.0481
Power (MWth)	49.89	50
Efficiency Design Point (%)	60.01	-
Mean Annual Efficiency (%)	54.80	55.63
Reflective Surface Area (m^2)	152,270.72	136,011.51
Annual Energy (MWht)	150,768.00	149,560.720
System Cost ($)	40,652,834.350	41,253,240.000

An appropriate design point at the identified site (Latitude: 12.39° N Longitude: 7.60° E) is selected during the summer solstices, signifying a high sun position. It should, however, be noted that the DNI frequency distribution (in the form of a sun path diagram) shows the date for high sun position at the identified site is not the usual summer solstice date of June 21st for locations north of the equator, but instead on April 20th. A DNI design point power of 640 W/m^2 was chosen. The value represents a safe threshold of thermal rating, which the receiver will not exceed, thereby ensuring appropriate sizing.

For a 50 MWth field, the LCOH obtained was 0.0474 $/kWh, with the annual thermal energy at 150,768.00 MWth, and the total field cost at $40,652,834.350. The mean annual efficiency for the designed and optimized plant was 54.80%. In order to further validate the model developed, SAM was used to generate and optimize a 50 MWth field. The results were then compared with the model developed. To calculate the LCOH using SAM, Equation (22) was applied using the same values for the CRF. The comparison between the results is shown again in Table 3. A marginal difference was observed in the LCOH from both models, showing a good correlation.

In Figure 7, the field layout from the conventional field model is shown, representing the mean annual heliostat efficiency.

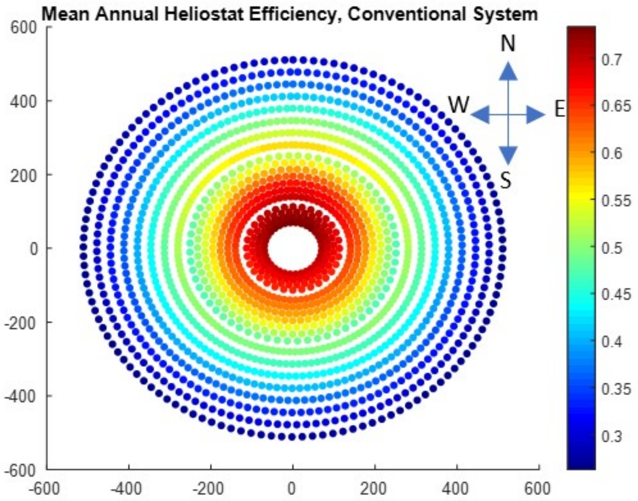

Figure 7. Field layout of a 50 MWth Conventional Power Tower System.

3.2. Multi-Tower Field

In the multi-tower field, one of the first questions to address is the position in which the auxiliary tower will be placed. The auxiliary tower location was calculated based on the region with the lowest efficiency and reflected energy. The average annual heliostat efficiency representation of the field was evaluated to aid in identifying the region with the lowest efficiency. In order to simplify the computation, the field was divided only into four quadrants when computing the position of the auxiliary tower as shown in Figure 8. The results are tabulated in Table 4.

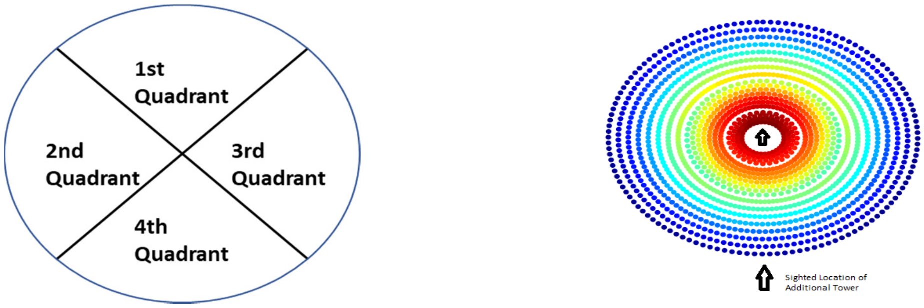

(a) (b)

Figure 8. (**a**) Position of the four identified quadrants in the field. (**b**) Description of the region in which the additional tower would be sighted.

Table 4. Mean annual efficiency at the four identified quadrants.

Averaged Annual Efficiency in the 1st Quadrant (%)	Averaged Annual Efficiency in the 2nd Quadrant (%)	Averaged Annual Efficiency in the 3rd Quadrant (%)	Averaged Annual Efficiency in the 4th Quadrant (%)
57.14	56.24	54.37	53.37

The results in Table 4 clearly show the region with the least mean annual efficiency value. This is predominantly a result of the more substantial cosine losses in that region of the field. This corroborates evidence that plant locations north of the equator favour north-facing fields [36,38]. The additional tower to be introduced into the field is hence sited at the central position of the weakest quadrant, the 4th quadrant (see Figure 8b).

With the multi-tower field now generated, the criteria for how the heliostats aim at the receivers in the field were defined. The heliostats are not restricted in terms of which tower they are allowed to focus on. Each heliostat makes a decision about the receiver to aim at based on the strength of the reflected radiation. In other words, optical efficiency losses are computed for each heliostat in the two scenarios: aiming at the central tower and aiming at the auxiliary tower. The aim point bearing the lesser loss, for all the combined optical efficiency loss parameters, is selected.

An overall assessment of the potential of adding an auxiliary tower to the 50 MWth optimized conventional field was conducted. This assessment can be considered as an evaluation for upgrading or retrofitting a pre-existing conventional field. The auxiliary tower was added under varying receiver dimensions, tower height and tower displacement distance. Variables' ranges for the auxiliary tower are highlighted in Table 5. The results in Figure 9a,b show an evident increase in the field efficiency values and the thermal energy for different combinations of additional tower input variables (Table 5). In Figure 9a, at no point does the LCOH of the field with the auxiliary tower and converge with the conventional field, signifying that at that particular field power, the auxiliary tower would always have a higher LCOH. With increasing values of the design variables, the LCOH of the auxiliary tower becomes higher (Figure 9a).

Table 5. Multi-tower (one additional tower) field model design variables with lower and upper bounds.

Design Variables	Variables Range
Number of Heliostats in 1st row (Zone 1)	10–46
Heliostat Area (m^2)	25–120
Receiver Dimensions (m^2)	25–226
Tower Height (m)	25–140
Heliostat Row Separation Distance Zone 1 (m)	(0.866–1.666) × DM
Heliostat Separation Distance Zone 2 (m)	(0.866–2.666) × DM
Heliostat Separation Distance Zone 3 (m)	(0.866–3.666) × DM
Additional Tower Placement Distance (m)	((0.866–1.666) × DM) + Df
Additional Tower Height (m)	25–140
Additional Tower Receiver Dimensions (m^2)	25–226

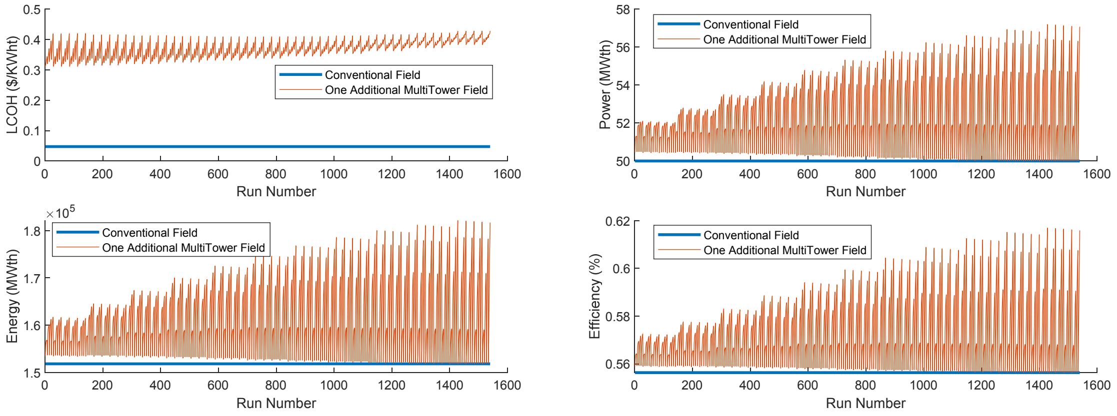

(**a**) (**b**)

Figure 9. (**a**) Levelized Cost of Heat (LCOH) and energy output with one additional multi-tower system (**b**) thermal power and mean annual efficiency with one additional multi-tower system.

The additional design variables for the multi-tower configuration were utilized in the optimization process for the 50 MWth field with the same objective function of LCOH highlighted earlier. This increased the number of design variables used in the optimization process. The updated number of design variables is highlighted in Table 5.

Here, Df is the final distance between the central tower and the furthest heliostat in the same-axis direction of the auxiliary tower.

In the multi-tower setup, the same objective function as the conventional field was used: minimizing the LCOH. However, in order to simplify the solution process, additional objectives were added and handled as constraints. These include the total heliostat reflective surface area and the field efficiency. This is in addition to the initial constraint limiting the optimizer to computing results only at a field power of 50 MWth. For the field efficiency, only values that are higher than the computed result from the conventional setup are considered in the optimizer. The total reflective surface area, on the other hand, limits the optimizer from finding solutions that exceed the total reflective surface area of the conventional field. After a certain number of repeated optimizations runs, the minimal value of LCOH was recorded, after achieving a low spread between the lowest and highest value of the objective function [62].

4. Results and Discussion

The results from the optimization process are highlighted in Table 6. In order to provide a comparative description, the results from the multi-tower field are compared to the results from an optimized single-tower conventional field. The results are all tabulated in Table 6.

Table 6. Results: Conventional field, and multi-tower field.

Parameter	Conventional Field	Multi-Tower Field (One Additional Tower)
Heliostat Area (m^2)	95.17	93.99
Central Tower Height (m)	91.48	92.91
Central Receiver Area (m^2)	55.84	40.36
Auxiliary Tower Height (m)	-	92.94
Auxiliary Receiver Area (m^2)	-	66.38
LCOH ($/kWht)	0.0474	0.0579
Field Power (MWth)	49.89	49.79
Efficiency Design Point (%)	60.01	62.95
Mean Annual Efficiency (%)	54.80	58.44
Mean Annual Attenuation Efficiency (%)	96.52	97.07
Mean Annual Shadowing and Blocking Efficiency (%)	95.96	96.84
Mean Annual Cosine Efficiency (%)	77.84	84.47
Mean Annual Interception Efficiency (%)	87.82	92.70
Reflective Surface Area (m^2)	152,270.72	140,987.00
Number of Heliostats	1600	1500
Annual Energy (MWht)	150,768.00	153,788.27
Auxiliary Receiver Thermal Power (MWth)	-	11.51
System Cost ($)	40,652,834.35	57,198,009.00

As shown in Table 6, the additional tower for the multi-tower field results in a marked increase in the optical field efficiency value. A 3.64% increase in the mean annual field efficiency and a 2.94% increase in the design point efficiency is observed when compared to the results obtained in a conventional field setup. The most considerable improvement in optical efficiency is seen in the cosine efficiency value. This is primarily because the additional tower in the field provides an alternate aim point for the heliostats with the least reflecting efficiency.

The LCOH, however, is higher in the new configuration. This indicates that the benefits due to the increment in the optical efficiency values and annual energy output do not outweigh the cost of installing an additional tower and receiver.

In the new configuration, the number of heliostats aiming at the one auxiliary tower changes through the months and through the day (see Figure 10). At the design point date, April 20th, a total number of 317 heliostats aim at the auxiliary tower at solar noon (Figure 10a). The number of heliostats aiming at the auxiliary tower at solar noon peaks in January and December, when the sun's position is low, making it difficult for the 'weak' heliostats to reflect radiation onto the main central tower without incurring enormous cosine losses (Figure 10a). On the other hand, during sunshine hours, and at around solar noon, a reduced number of heliostats aim at the auxiliary tower (Figure 10b). This is predominately due to the lesser cosine losses from the heliostats aiming at the main central tower, hence the central tower becomes a preferred target.

The computed thermal power rating of the auxiliary tower was 11.51 MWth. The main central tower, which caters to the bulk of the heliostats in the field, now has a computed thermal rating of 38.28 MWth.

In Figure 11a,b, the month-on-month variation of the total energy output and mean efficiency values for both the conventional field and the multi-tower field is shown. A marked improvement in the mean efficiency value was observed from January to December in the two models shown in

Figure 11b. In Figure 11a, it is worth mentioning that the dip witnessed during months 6–8 is a result of the poor DNI values, as a result of cloud cover during that period (from NiMet data).

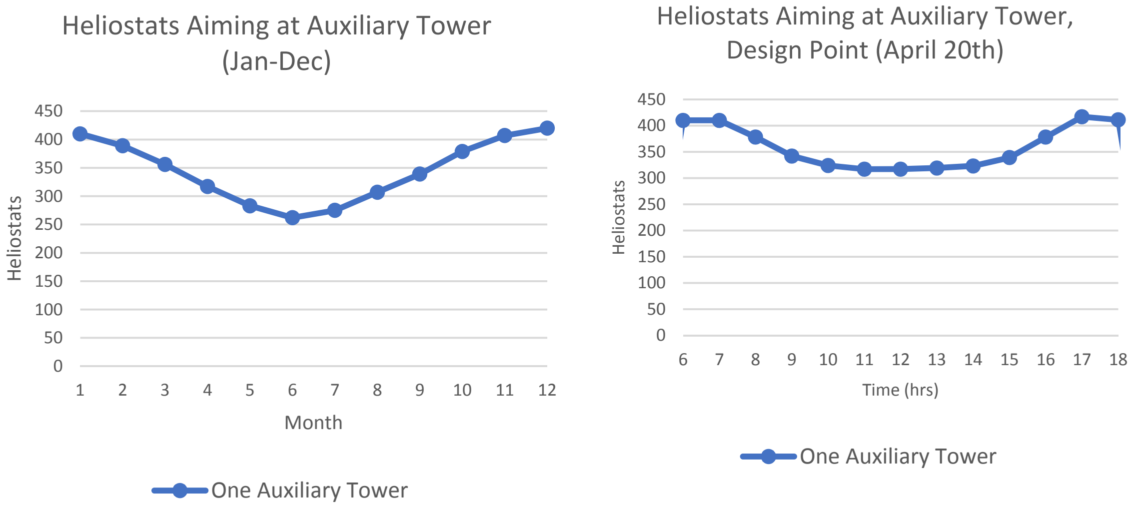

(**a**) (**b**)

Figure 10. (**a**) Heliostats aiming at the auxiliary tower through the year; (**b**) Heliostats aiming at the auxiliary tower during sunshine hours at the design point date.

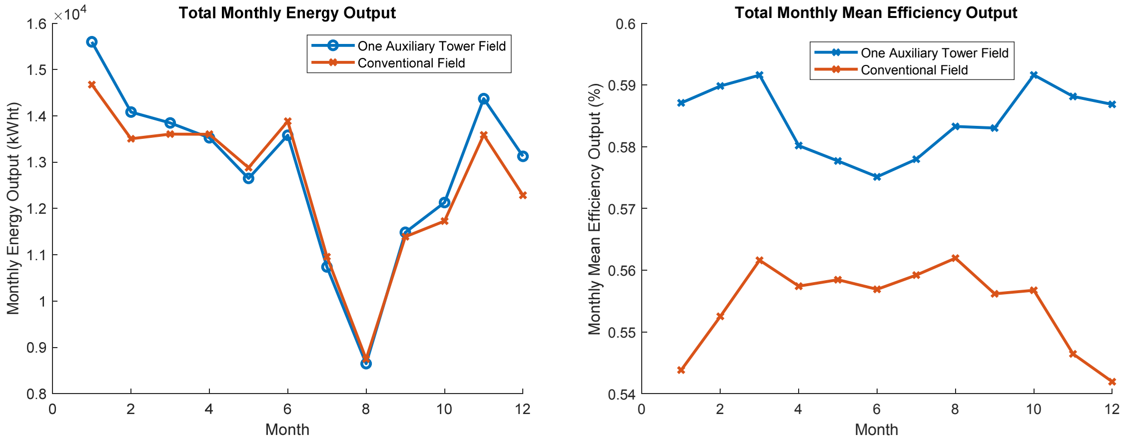

(**a**) (**b**)

Figure 11. (**a**) Total monthly energy output, conventional and one additional tower field; (**b**) Total monthly mean efficiency output, conventional and one additional tower field.

A more explicit demonstration of the effect of the multi-tower field is shown in Figure 12. The mean annual efficiency field layout for the conventional system and the one additional tower field is seen in Figure 12a,b. The change in shading matrices of the optical losses model from the conventional field to the multi-tower field is shown in Figure 12c–i.

The entire optimization for the multi-tower field was initially made for a 50 MWth field. A broader range of thermal power was examined, so a more critical analysis of the effect of a multi-tower field can be observed. Figure 13 shows the LCOH results from both the conventional field model and the multi-tower field model at various-power thermal field values.

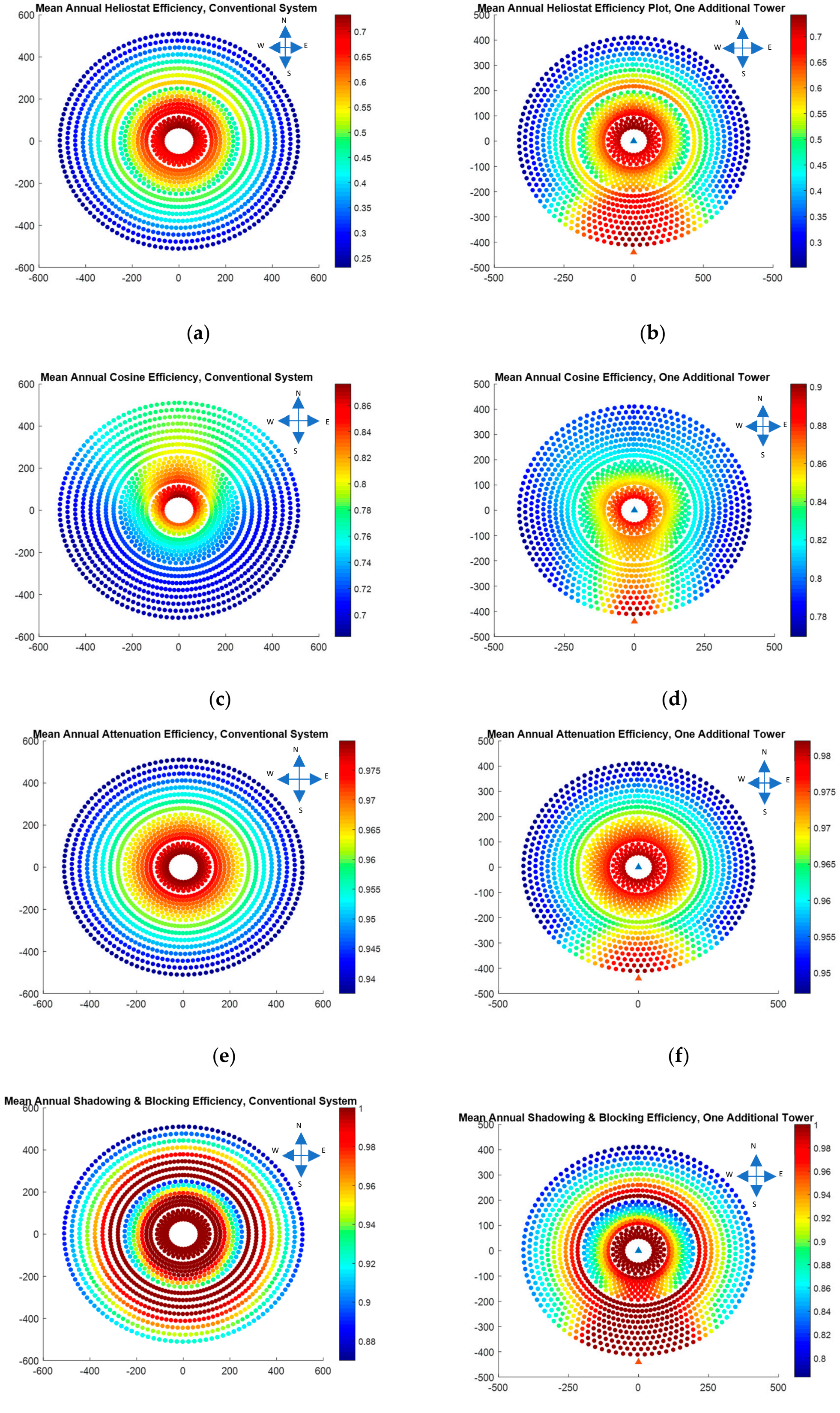
Mean Annual Heliostat Efficiency, Conventional System

Mean Annual Heliostat Efficiency Plot, One Additional Tower

Mean Annual Cosine Efficiency, Conventional System

Mean Annual Cosine Efficiency, One Additional Tower

Mean Annual Attenuation Efficiency, Conventional System

Mean Annual Attenuation Efficiency, One Additional Tower

Mean Annual Shadowing & Blocking Efficiency, Conventional System

Mean Annual Shadowing & Blocking Efficiency, One Additional Tower

(**a**) (**b**)

(**c**) (**d**)

(**e**) (**f**)

(**g**) (**h**)

Figure 12. *Cont.*

(**g**) (**h**)

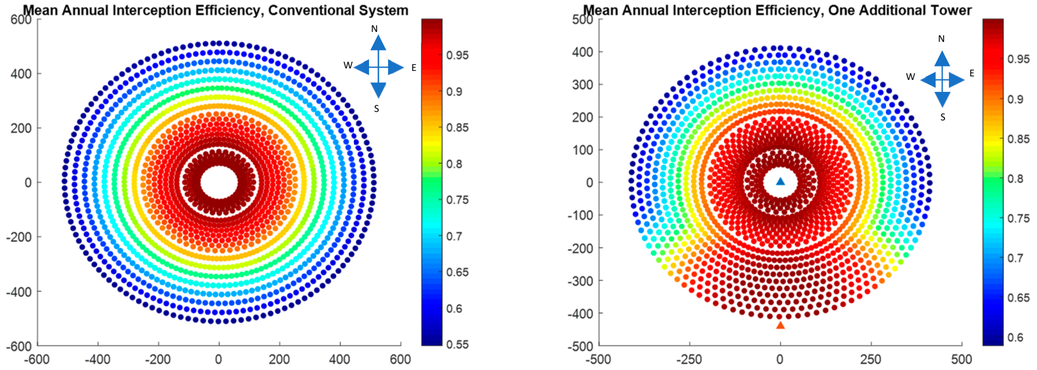

(**i**) (**j**)

Figure 12. (**a**,**c**,**g**,**i**) Conventional field: mean annual efficiency, cosine, attenuation, shadowing & blocking and interception efficiency respectively. (**b**,**d**,**f**,**h**,**j**) Multi-tower field, one additional tower: mean annual efficiency, cosine, attenuation, shadowing and blocking and interception efficiency respectively.

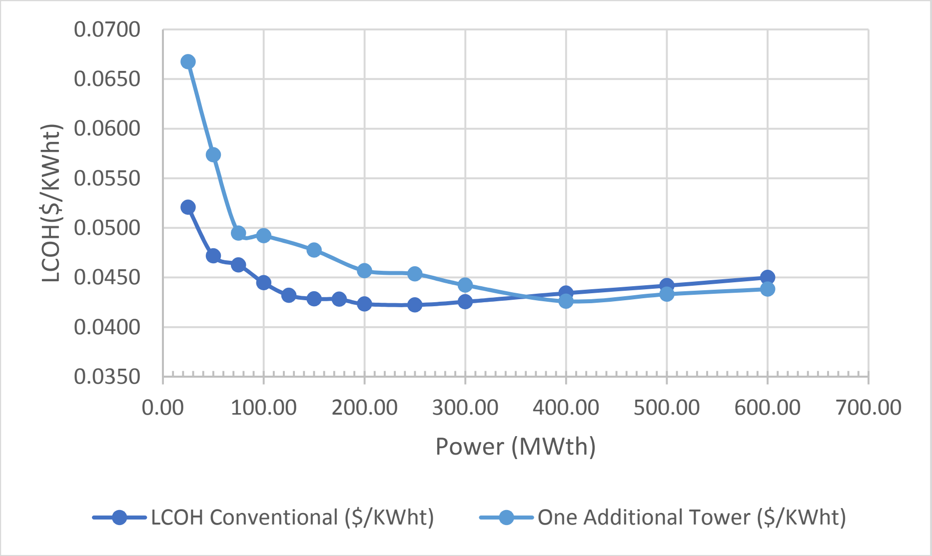

Figure 13. Levelized Cost of Heat (LCOH) for a conventional field and a multi-tower field.

Results from Figure 13 clearly show the promising LCOH trend of multi-tower fields at higher thermal power figures and larger fields. In larger fields, a higher number of weaker heliostats are witnessed in the field, making the need for and use of an additional tower all the more critical. The heliostats at the weaker region of a multi-tower field are provided with an additional tower to reflect the sun's radiation, thereby considerably cutting down on cosine, spillage and attenuation losses which in turn gives rise to higher total energy output. At a certain point, as seen in the trend, the multi-tower field continuously provides a lower LCOH value compared to a conventional field of similar thermal power. This is seen explicitly at the 400 MWth range in the one auxiliary tower configuration, where expanding the conventional field in order to attain a higher thermal field output becomes less effective due to the significant optical losses gained as a result of the size of the field.

5. Conclusions

In power tower systems, the heliostat field is one of the essential subsystems, comprising 40%–50% of the plant's total investment cost and of about 40% of the plant's overall power losses. Different field configurations are therefore being investigated. Multi-tower systems provide an alternative approach in which the heliostat field efficiencies can be increased. In this paper, a different architecture of the multi-tower configuration is investigated. The configuration explored, which provides a different take to the usual mainstream multi-tower configuration, involves adding an auxiliary tower to an existing surrounding conventional field.

As a case study, the multi-tower configuration was applied in Katsina, Nigeria, and the field parameters were optimized for 50 MWth field power. To identify the position in which the auxiliary tower was sighted, the mean annual field efficiency of the 50 MWth conventional field was computed. The results clearly showed that the southern region, which had heliostats with huge cosine losses, had the least mean annual efficiency value of heliostats. The presence of the auxiliary tower provided an overall increase in the system efficiency of the field by reducing some of the losses entailed in a conventional single-tower setup, by providing the 'weaker' heliostats in the region a more favourable tower to target. A reduction in attenuation, spillage and cosine losses by 0.55%, 4.88% and 6.63%, respectively, was observed in the multi-tower configuration. This led to an overall increase in the mean annual efficiency of the field by 3.64%.

With most heliostats on the multi-tower configuration targeting the main central tower in the 50 MWth field, the auxiliary tower's contribution to the LCOH becomes limited. This can be seen in the small increment of 3020MWht recorded in the thermal field energy output. The LCOH is thus higher in the new configuration. This indicated that the size of the field limits the potential contribution of the auxiliary tower at 50 MWth. Similarly, the benefits due to the increment in the optical efficiency values and annual energy output do not out-weigh the cost of installing an additional tower and receiver.

In larger fields, a more significant number of weak heliostats are witnessed. The poorly reflecting heliostats are provided with an additional tower to reflect the solar radiation to, thereby considerably cutting down on some optical losses, which in turn gives rise to higher energy output. A continuous reduction in the LCOH for larger fields is seen as a result. At a thermal field power rating of 400 MWth, the multi-tower configuration provides a higher LCOH compared to a conventional field with similar power.

The growth and development of power tower systems has seen larger systems, up to 150MWe, being built around the world. The multi-tower configuration provides a viable alternative way in which such large power tower systems can be built, by potentially providing a lower LCOH and higher plant efficiency. The configuration could also be applied in existing fields by updating or retrofitting existing conventional fields and adding auxiliary towers. The study here provides a quick overview of auxiliary towers in a multi-tower field configuration. In further studies, the effect of the field configuration on the whole plant, especially on the storage subsystem, can be investigated. Furthermore, techniques for developing the field by reconfiguring the field layout to reflect the multi-towered setup can also be studied in future work.

Author Contributions: P.K., C.S. and Z.A.H. are responsible for the conceptualization, methodology, formal analysis, and investigation of the project. Z.A.H. is responsible for model development, writing the original article draft and data visualization. P.K. is responsible for technical support, model analysis and validation. P.K. and C.S. are responsible for the project administration, funding acquisition, resources, and reviewing and editing the article. All authors have read and agreed to the published version of the manuscript.

Funding: The research was funded by the Petroleum Technology Development Fund (PTDF) in Nigeria as part of oversees scholarship scheme on sustainable energy research.

Conflicts of Interest: The authors declare no conflict of interest.

References

1. Behar, O.; Khellaf, A.; Mohammedi, K. A review of studies on central receiver solar thermal power plants. *Renew. Sustain. Energy Rev.* **2013**, *23*, 12–39. [CrossRef]
2. IEA. Technology Roadmap Solar Thermal Electricity. *Int. Energy Agency* **2014**, *52*. [CrossRef]

3. Weinrebe, G.; von Reeken, F.; Wöhrbach, M.; Plaz, T.; Göcke, V.; Balz, M. Towards Holistic Power Tower System Optimization. *Energy Procedia* **2014**, *49*, 1573–1581. [CrossRef]
4. Mills, D. Advances in solar thermal electricity technology. *Sol. Energy* **2004**, *76*, 19–31. [CrossRef]
5. IRENA. Renewable Energy Technologies Cost Analysis Series: Concentrating Solar Power. *Compr. Renew. Energy* **2012**, *3*, 595–636. [CrossRef]
6. Kolb, G.; Ho, C.; Mancini, T.; Gary, J. Power tower technology roadmap and cost reduction plan. *Sandia* **2011**, *38*. [CrossRef]
7. International Renewable Energy Agency (IRENA). *Renewable Power Generation Costs in 2018*; IRENA: Abu Dhabi, UAE, 2018.
8. Noone, C.J.; Torrilhon, M.; Mitsos, A. Heliostat field optimization: A new computationally efficient model and biomimetic layout. *Solar Energy* **2012**, *86*, 792–803. [CrossRef]
9. Kolb, G.J.; Jones, S.A.; Donnelly, M.W.; Gorman, D.; Thomas, R.; Davenport, R.; Lumia, R. *Heliostat Cost Reduction Study*; Sandia National Laboratories: Albuquerque, NM, USA, 2007; Volume SAND2007-3. [CrossRef]
10. Cádiz, P.; Frasquet, M.; Silva, M.; Martínez, F.; Carballo, J. Shadowing and Blocking Effect Optimization for a Variable Geometry Heliostat Field. *Energy Procedia* **2015**, *69*, 60–69. [CrossRef]
11. Wei, X.; Lu, Z.; Wang, Z.; Yu, W.; Zhang, H.; Yao, Z. A new method for the design of the heliostat field layout for solar tower power plant. *Renew. Energy* **2010**, *35*, 1970–1975. [CrossRef]
12. Cruz, N.C.; Redondo, J.L.; Berenguel, M.; Álvarez, J.D.; Becerra-Teron, A.; Ortigosa, P.M. High performance computing for the heliostat field layout evaluation. *J. Supercomput.* **2016**, *73*, 1–18. [CrossRef]
13. Collado, F.J.; Guallar, J. Campo: Generation of regular heliostat fields. *Renew. Energy* **2012**, *46*, 49–59. [CrossRef]
14. Aldulaimi, K.M.; Söylemez, M.S. Performance Analysis of Multilevel Heliostat Field Layout. *Turk. J. Sci. Technol.* **2016**, *11*, 11–20.
15. Besarati, S.M.; Yogi Goswami, D.; Stefanakos, E.K. Optimal heliostat aiming strategy for uniform distribution of heat flux on the receiver of a solar power tower plant. *Energy Convers. Manag.* **2014**, *84*, 234–243. [CrossRef]
16. Buck, R. Heliostat Field Layout Improvement by Nonrestricted Refinement. *J. Sol. Energy Eng.* **2013**, *136*, 21014. [CrossRef]
17. Carrizosa, E.; Domínguez-Bravo, C.; Fernández-Cara, E.; Quero, M. A heuristic method for simultaneous tower and pattern-free field optimization on solar power systems. *Comput. Oper. Res.* **2015**, *57*, 109–122. [CrossRef]
18. Carrizosa, E.; Domínguez-Bravo, C.-A.; Fernández-Cara, E. An optimization tool to design the field of a solar power tower plant allowing heliostats of different sizes. *Int. J. Energy Res.* **2017**. [CrossRef]
19. Lazardjani, M.Y.; Kronhardt, V.; Dikta, G.; Göttsche, J. Simultaneous optimization of micro-heliostat geometry and field layout using a genetic algorithm. In Proceedings of the AIP Conference, Cape Town, South Africa, 14–18 May 2016; Volume 1734. [CrossRef]
20. Danielli, A.; Yatir, Y.; Mor, O. Improving the optical efficiency of a concentrated solar power field using a concatenated micro-tower configuration. *Sol. Energy* **2011**, *85*, 931–937. [CrossRef]
21. Cruz, N.C.; Salhi, S.; Redondo, J.L.; Álvarez, J.D.; Berenguel, M.; Ortigosa, P.M. Design of a parallel genetic algorithm for continuous and pattern-free heliostat field optimization. *J. Supercomput.* **2018**, 1–16. [CrossRef]
22. Arrif, T.; Benchabane, A.; Germoui, M.; Bezza, B.; Belaid, A. Optimisation of heliostat field layout for solar power tower systems using iterative artificial bee colony algorithm: A review and case study. *Int. J. Ambient Energy* **2018**, 1–16. [CrossRef]
23. Deng, L.; Wu, Y.; Guo, S.; Zhang, L.; Sun, H. Rose pattern for heliostat field optimization with a dynamic speciation-based mutation differential evolution. *Int. J. Energy Res.* **2019**, 1–20. [CrossRef]
24. Romero, M.; Marcos, M.J.; Téllez, F.M.; Blanco, M.J.; Fernández, V.; Baonza, F.; Berger, F. Distributed power from solar tower systems: A MIUS approach. *Sol. Energy* **1999**, *67*, 249–264. [CrossRef]
25. Schramek, P.; Mills, D.R. Multi-tower solar array. *Sol. Energy* **2003**, *75*, 249–260. [CrossRef]
26. Augsburger, G.; Favrat, D. From Single- to Multi-Tower Solar Thermal Power Plants: Investigation of the Thermo-Economic Optimum Transition Size. In Proceedings of the SolarPACES 2012 Conference on Concentrating Solar Power and Chemical Energy Systems, Marrakesh, Morocco, 11–14 September 2012.
27. Pacheco, J.E.; Moursund, C.; Rogers, D.; Wasyluk, D. *Conceptual Design of a 100 MWe Modular Molten Salt Power Tower Plant*; eSolar, Inc.: Burbank, CA, USA, 2011.

28. Tyner, C.; Wasyluk, D. eSolar's Modular, Scalable Molten Salt Power Tower Reference Plant Design. *Energy Procedia* **2014**, *49*, 1563–1572. [CrossRef]
29. Piroozmand, P.; Boroushaki, M. A computational method for optimal design of the multi-tower heliostat field considering heliostats interactions. *Energy* **2016**, *106*, 240–252. [CrossRef]
30. Wood, C.; Drewes, K. Vast Solar: Improving performance and reducing cost and risk using high temperature modular arrays and sodium heat transfer fluid. In Proceedings of the SolarPaces Conference, Daegu, South Korea, 1–4 October 2019.
31. Duffie, J.A.; Beckman, W.A. *Solar Engineering of Thermal Processes*, 4th ed.; John Wiley & Sons Inc.: Hoboken, NJ, USA, 2013.
32. National Aeronautic and Space Agency (NASA). Surface Metreology and Solar Energy. Available online: http://eosweb.larc.nasa.gov/cgi-bin/sse/sse.cgi?+s01#s01 (accessed on 9 September 2011).
33. Ogunmodimu, O.; Marquard, A. CSP Technology and its Potential Contribution to Electricity Supply in northern Nigeria. *Int. J. Renew. Energy Res.* **2013**, *3*, 529–537. Available online: http://www.ijrer.com/index.php/ijrer/article/view/688 (accessed on 20 February 2020).
34. Habib, S.L.; Idris, N.; Ladan, M.; Mohammad, A. Unlocking Nigeria's Solar PV and CSP Potentials for Sustainable Electricity Development. *Int. J. Sci. Eng. Res.* **2012**, *3*, 1–8.
35. Ortega, G.; Rovira, A. Proposal and analysis of different methodologies for the shading and blocking efficiency in central receivers systems. *Sol. Energy* **2017**, *144*, 475–488. [CrossRef]
36. Stine, B.W.; Geyer, M. Power from the Sun. 2001. Available online: http://www.powerfromthesun.net/book.html (accessed on 16 June 2017).
37. Besarati, S.M.; Yogi Goswami, D. A computationally efficient method for the design of the heliostat field for solar power tower plant. *Renew. Energy* **2014**, *69*, 226–232. [CrossRef]
38. Wagner, M.J. Simulation and Predictive Performance Modeling of Utility-Scale Central Receiver System Power Plants. 2008. Available online: http://sel.me.wisc.edu/publications/theses/wagner08.zip (accessed on 12 November 2019).
39. Weijie, D.; Xuemei, Z. Modeling and Simulation of Heliostats Field in Solar Power Tower. In Proceedings of the 29th Chinese Control And Decision Conference (CCDC), Chongqing, China, 28–30 May 2017; pp. 3246–3251.
40. Sassi, G. Some notes on shadow and blockage effects. *Sol. Energy* **1983**, *31*, 331–333. [CrossRef]
41. Collado, F.J.; Turégano, J.A. Calculation of the annual thermal energy supplied by a defined heliostat field. *Sol. Energy* **1989**, *42*, 149–165. [CrossRef]
42. Ballestrín, J.; Marzo, A. Solar radiation attenuation in solar tower plants. *Sol. Energy* **2012**, *86*, 388–392. [CrossRef]
43. Leary, P.L.; Hankins, J.D. *User's Guide for MIRVAL: A Computer Code for Comparing Designs of Heliostat-Receiver Optics for Central Receiver Solar Power Plants*; Sandia National Lab.: Livermore, CA, USA, 1976. [CrossRef]
44. Schmitz, M.; Schwarzbözl, P.; Buck, R.; Pitz-Paal, R. Assessment of the potential improvement due to multiple apertures in central receiver systems with secondary concentrators. *Sol. Energy* **2006**, *80*, 111–120. [CrossRef]
45. García, L.; Burisch, M.; Sanchez, M. Spillage Estimation in a Heliostats Field for Solar Field Optimization. *Energy Procedia* **2015**, *69*, 1269–1276. [CrossRef]
46. Collado, F.J.; Gómez, A.; Turégano, J.A. An analytic function for the flux density due to sunlight reflected from a heliostat. *Sol. Energy* **1986**, *37*, 215–234. [CrossRef]
47. Collado, F.J. One-point fitting of the flux density produced by a heliostat. *Sol. Energy* **2010**, *84*, 673–684. [CrossRef]
48. Schwarzbözl, P.; Pitz-Paal, R.; Schmitz, M. Visual HFLCAL—A Software Tool for Layout and Optimisation of Heliostat Fields. 2009. Available online: http://elib.dlr.de/60308/ (accessed on 19 June 2017).
49. Collado, F.J.; Guallar, J. A review of optimized design layouts for solar power tower plants with campo code. *Renew. Sustain. Energy Rev.* **2013**, *20*, 142–154. [CrossRef]
50. Siala, F.M.F.; Elayeb, M.E. Mathematical formulation of a graphical method for a no-blocking heliostat field layout. *Renew. Energy* **2001**, *23*, 77–92. [CrossRef]
51. Collado, F.J.; Guallar, J. Quick design of regular heliostat fields for commercial solar tower power plants. *Energy* **2019**, *178*, 115–125. [CrossRef]
52. Gabbrielli, R.; Castrataro, P.; Del Medico, F.; Di Palo, M.; Lenzo, B. Levelized cost of heat for linear Fresnel concentrated solar systems. *Energy Procedia* **2014**, *49*, 1340–1349. [CrossRef]

53. Louvet, Y.; Fischer, S.; Furbo, S.; Giovanetti, F.; Mauthner, F.; Mugnier, D.; Veynandt, F. LCOH for Solar Thermal Applications. 2017. Available online: http://task54.iea-shc.org/ (accessed on 4 December 2019).
54. Baez, M.J.; Martinez, T.L. Technical Report on the Elaboration of a Cost Estimation Methodology. Available online: http://www.front-rhc.eu/wp-content/uploads/2014/11/FROnT_D3.1_elaboration-of-a-cost-estimation-methodology_2015.07.22.pdf (accessed on 5 November 2019).
55. Collado, F.J.; Guallar, J. Two-stages optimised design of the collector field of solar power tower plants. *Sol. Energy* **2016**, *135*, 884–896. [CrossRef]
56. Taylor, M.; Daniel, K.; So, E.Y. IRENA: Renewable Power Generation Costs in 2014. 2014. Available online: https://www.irena.org/documentdownloads/publications/irena_re_power_costs_2014_report.pdf (accessed on 12 November 2019).
57. Kistler, B.L. *A User's Manual for DELSOL3: A Computer Code for Calculating the Optical Performance and Optimal System Design for Solar Thermal Central Receiver Plants*; SANDIA National Laboratories: Albuquerque, NM, USA, 1986.
58. NREL. *System Advisor Model (SAM)*; NREL: Golden, CO, USA, 2014.
59. Turchi, C.S.; Heath, G.A. Molten Salt Power Tower Cost Model for the System Advisor Model (SAM) Molten Salt Power Tower Cost Model for the System Advisor Model (SAM). *Energy* **2013**. [CrossRef]
60. Talebizadeh, P.; Mehrabian Ali, M.; Rahimzadeh, H. Optimization of Heliostats Layout in Central Receiver Solar Power Plants. *J. Energy Eng.* **2014**, *140*, 04014005. [CrossRef]
61. Atashkari, K.; Nariman-Zadeh, N.; Pilechi, A.; Jamali, A.; Yao, X. Thermodynamic Pareto optimization of turbojet engines using multi-objective genetic algorithms. *Int. J. Therm. Sci.* **2005**, *44*, 1061–1071. [CrossRef]
62. Pitz-Paal, R.; Botero, N.B.; Steinfeld, A. Heliostat field layout optimization for high-temperature solar thermochemical processing. *Sol. Energy* **2011**, *85*, 334–343. [CrossRef]